Journal of Ocean Engineering and Science 10 (2025) 366–378

Contents lists available at ScienceDirect

Journal of Ocean Engineering and Science

journal homepage: www.elsevier.com/locate/joes

Large eddy simulation of plunging solitary wave: Understanding the breaking and turbulent mechanisms along shoaling region

Abbasali Rahmani[a,b], Alireza Keramat[a,b,*], Jinghua Wang[a,b], Huan-Feng Duan[a,b]

[a] Department of Civil and Environmental Engineering, The Hong Kong Polytechnic University, Hung Hom, Kowloon, Hong Kong Special Administrative Region 999077

[b] Research Institute of Sustainable Urban Development, The Hong Kong Polytechnic University, Hung Hom, Kowloon, Hong Kong Special Administrative Region 999077

ARTICLE INFO

Article history:
Received 5 March 2023
Revised 23 May 2023
Accepted 27 July 2023
Available online 8 August 2023

Keywords:
Plunging solitary wave
Breaking wave vortices
Large eddy simulation
Sub-grid scale models
Turbulent kinetic energy
Hydrodynamics
Shoaling zone

ABSTRACT

A large eddy simulation (LES) is conducted to investigate the distribution of turbulence kinetic energy (TKE) under a plunging solitary wave over a 1:15 slope. This study provides a novel contribution to the field by examining the roles of resolved and sub-grid scale TKE in plunging solitary waves at the different stages of wave breaking. Furthermore, comparing the performances of two sub-grid scale (SGS) models in simulating the distribution of TKE was carried out to identify their performances. The separate investigation of these components in the context of wave breaking and recognizing the importance of an appropriate sub-grid scale model to consider the effects of small-scale eddies provide a significant advancement in understanding coastal morphological changes and nearshore sediment transport. Both the zero-equation and one-equation SGS models demonstrated acceptable performance in simulating water surface and kinematic properties. The one-equation SGS model, however, provided more accurate results on TKE transport during the breaking process and as the wave approaches its collapsing point. The study's results reveal that an SGS model's inability to simulate TKE transport (such as in the zero equation model) leads to inaccurate simulations of the TKE level and breaking location in the breaking zone. Additionally, the results of the one-equation model demonstrated that the maximum horizontal fluid velocity around the wavefront surface is a better predictor of breaking wave onset than the horizontal fluid velocity at the wave crest.

1. Introduction

Turbulence kinetic energy (TKE) is a term used to describe the amount of energy involved in a turbulent fluid motion. The turbulent flow produced by wave breaking significantly impacts nearshore sediment transport, coastal morphological changes, and mixing processes. Using computational fluid dynamics (CFD), a numerical flow field simulation is one method for obtaining TKE in this situation. TKE can be acquired as an outcome in these models, providing information about the intensity and distribution of turbulence in the water column. Combining the TKE results with sediment transport models can estimate sediment transport rates and patterns. Despite recent advances in the understanding of the breaking process, the complex interaction between the turbulent flow, air entrainment, and water surface has yet to be fully comprehended [1].

Previous studies have analyzed the hydrodynamic effects of a single wave on the flow characteristics in the shoaling zone and during wave propagation using one, two, or three-dimensional approaches, depending on their specific objectives [2,3]. Since the vortices induced by wave breaking exhibit three-dimensional characteristics, our study employs a three-dimensional analysis to comprehensively investigate the hydrodynamic effects of a solitary wave on the water flow during wave propagation and shoaling conditions.

Breaking is considered the most significant of the various mechanisms that dissipate wave energy, as it is directly driven by wave-induced hydrodynamic forces [4,5]. Structurally, the breaking process and wave collapse are distinct phenomena. Breaking is primarily caused by the hydrodynamic forces induced by the wave while collapsing is further driven by gravity and inertia due to the transfer of water mass in the wave. These differences in physics have

* Corresponding author.
E-mail address: alireza.keramat@polyu.edu.hk (A. Keramat).

https://doi.org/10.1016/j.joes.2023.07.008

essential implications for the dynamics and behavior of waves as they approach the shore [4].

The formation and behavior of turbulence structures during wave breaking are important factors affecting coastal sediment transport and nearshore morphology. Laboratory measurements and experimental observations have shed light on the complex dynamics of wave-breaking-induced turbulence, revealing the formation and rapid breakdown of vortices behind the wave crest [6]. These vortices initially form with an axis of rotation parallel to the wave crest and rapidly break into three-dimensional turbulence structures [7]. Experimental observations confirmed the formation and breaking of the surface vortices by measuring the lag between the wave crest and the level of turbulence that followed it [8]. Turbulent kinetic energy (TKE) measures the energy stored in the turbulent motions of fluid particles. It is a useful measure for assessing turbulence intensity, as the formation and breakdown of eddies during wave breaking are detectable for only a brief period [8].

The turbulence generated by wave breaking is characterized by forming vortices, also known as large eddies, which play a crucial role in transporting turbulent kinetic energy (TKE). The surface-generated large eddies advect and diffuse TKE. According to experiments on nearshore region dynamics, TKE is transported landward and seaward under plunging and spilling wave breaking [9]. It is demonstrated that the wave breaking produces counter-rotating vortices, which are responsible for TKE downward transport [10]. Therefore, the large eddies play an important role in the generation and transport of TKE in the breaking wave. The TKE transport equation could explain the turbulence dynamics under the breaking process [11,12].

Reynolds Averaged Navier-Stokes (RANS) models are frequently employed for wave modeling [13–15]. However, the two-equation closure models are limited to zones with minor TKE effects. Two-equation RANS models are unconditionally unstable in some regions before and after wave breaking, resulting in wave breaking at different locations than observed in experiments [16–18]. This inaccuracy arises from the nonphysical overproduction of the TKE. In addition, these models merely obtain an average value of turbulent properties. Therefore, two-equation RANS models are not suitable for evaluating TKE precisely.

The most accurate replica of a natural fluid dynamic phenomenon can be made by direct numerical simulation (DNS), which solves Navier-Stokes equations for the smallest possible eddies. However, due to its computational costs, DNS is only available for small-scale flows, such as a wave boundary layer with low Reynolds numbers [19]. There is an intermediate idea in which large eddies are directly resolved, and closure models reproduce small eddies' effects. These models are named the Sub-Grid Scale (SGS) and Sub-Particle Scale in the case of the Eulerian and Lagrangian approaches, respectively. Concerning the direct simulation of large eddies, the performance of the Large Eddy Simulation (LES) approach for eddies containing a substantial portion of TKE is relatively close to that of DNS; thus, the LES approach is interested in breaking process simulation.

Two Eulerian and Lagrangian LES approaches are repeatedly utilized to investigate turbulent fields under breaking waves. Smooth Particle Hydrodynamic (SPH) methods are frequently used to model phenomena with high water surface gradients, such as wave breaking, and hydraulic jump [20–22]. Nevertheless, an SPH-based LES would require 16 times finer resolution than its Eulerian LES counterpart, which dictates high computational costs [23]. Thus, the Eulerian approach is preferred in this study.

Researchers have been interested in forming turbulent structures under breaking waves, how they transport, and what happens to them. An LES simulation of a breaking wave based on the Finite Volume Method (FVM) demonstrated that turbulence gradually spread down behind the spilling breaker. In contrast, in the strong plunging type, large eddies rapidly spread turbulence over the whole water depth [24]. Farahani and Dalrymple [25] performed an SPH-based LES to study turbulent vortical structures generated by broken solitary waves. Per experimental results [9], it has been discovered that for spilling breaking of a solitary wave, the vortex structures are left behind the crest; however, for plunging breaking, the formed vortices mitigate shoreward along with wave direction. Additionally, it is shown that surface-generated turbulence (TKE) prevails over bed-generated turbulence during the breaking process.

Continuing turbulence investigations of breaking solitary waves, Zhou et al. [26] used FVM-based LES simulation to simulate three-dimensional obliquely descending eddies caused by a spilling breaker. Additionally, this work outlined a procedure for converting beneath-surface instabilities into powerful, three-dimensional downburst vortices. The spilling type of breaking has received considerable attention, while studies on the turbulence generated by plunging breaking have been relatively limited. The focus of this study is on the investigation of the spreading of plunging-generated turbulence and evaluating its characteristics.

The studies conducted thus far on wave breaking have shown that large eddies play a crucial role in the formation and distribution of turbulence. These eddies are primarily generated by the instability of the free surface during the breaking phenomenon. The LES approach has proven more effective in accurately explaining the events associated with wave breaking.

This study makes numerous original contributions to the shoaling zone field. First, the research uses large eddy simulation (LES) with OpenFOAM to examine the turbulent structures caused by plunging solitary waves because plunging waves receive less attention than spilling waves. This work represents an approach to exploring plunging breaking wave dynamics. Second, the study compares how well the zero-equation and one-equation sub-grid scale (SGS) models simulate the distribution of turbulence kinetic energy (TKE) under a plunging solitary wave. This comparison reveals the effectiveness of SGS models in faithfully simulating wave breaking. Additionally, the study evaluates the performance of two distinct breaking onset kinematic criteria, namely the horizontal fluid velocity at the wave crest and the maximum horizontal fluid velocity, in predicting wave breaking. This assessment is based on the findings obtained from the one-equation SGS model. Finally, the one-equation SGS model is used to examine the distribution of TKE under a plunging solitary wave. The magnitudes of the resolved and unresolved (SGS) parts of the TKE are compared and ordered, providing new insights into the roles of these components in wave breaking. These original contributions advance our understanding of coastal morphological changes and nearshore sediment transport.

This work aims to provide a deeper understanding of the breaking and turbulent mechanisms along the shoaling region. By focusing on investigating a solitary breaking wave rather than a train of waves, it is possible to gain insights into wave-breaking mechanisms without the influence of preceding broken waves. As the plunging waves exhibit common characteristics, the study concentrates on a uniform slope bed that can accurately replicate plunging wave conditions.

This study offers a novel quantitative and qualitative evaluation of the role of TKE components by examining the various amounts of resolved and sub-grid-scale TKE in plunging solitary waves at various wave-breaking stages. The study highlights the significance of using an appropriate sub-grid-scale model to account for the effects of the small-scale eddies that are advected and diffused beneath the breaking wave. The research advances our understanding of turbulence transport under plunging waves by shedding light on the separate contributions of resolved and sub-grid-scale TKE.

The paper's outline is as follows: after presenting the mathematical model, two different sub-grid scale models are introduced, and their characteristics are presented in Section 2. Validation and simulation quality are assessed in Section 3, while Section 4 is allocated to the presentation and discussion of the results. The findings are summarized in Section 5.

2. Model description

Through the use of large eddy simulation, a three-dimensional turbulence-resolving technique is employed in this study. In the LES framework, the field of eddies is divided into resolved and unresolved parts by filtering the Navier-Stokes equation. Large-scale eddies are resolved using an appropriate grid size, while small-scale eddies are modeled using sub-grid scale models. The filtered partial differential equations are discretized using the finite volume approach. This numerical method is utilized to implement the mathematical model. Proper boundary and initial conditions are applied to simulate behavior as closely as possible to that of the wave flume.

In order to accurately track the water surface, the Volume Of Fluid (VOF) scheme is employed. The numerical computations are conducted using the open-source CFD toolbox, OpenFoam. The subsequent sections provide a detailed description of the mathematical and numerical models utilized in this study.

2.1. Mathematical model

Navier-Stokes equations have been exploited to describe the flow of two immiscible, incompressible fluids [24,27]. The LES approach is adopted to simulate turbulent flow due to the breaking wave through which the Navier-Stokes equations are filtered. Consequently, the filtered continuity and Navier-Stokes equations are presented as follows:

$$\frac{\partial \bar{u}_i}{\partial x_i} = 0 \tag{1}$$

$$\frac{\partial \bar{u}_i}{\partial t} + \frac{\partial \bar{u}_i \bar{u}_j}{\partial x_j} = -\frac{1}{\rho}\frac{\partial \bar{p}}{\partial x_i} + g_i + 2\nu\frac{\partial \bar{S}_{ij}}{\partial x_j} - \frac{\partial \tau^s_{ij}}{\partial x_j} \tag{2}$$

where $\bar{u}_i$, x_i, and g_i are filtered velocity, position vector, and the component of gravitational acceleration in i direction, respectively. Although, The indices i and j correspond to the components of vectors, with each index representing a specific direction or component of the vector. When used to represent a tensor, the indices i and j together denote the components of the tensor, with the first index specifying the row and the second index specifying the column in a matrix representation ($i, j = 1, 2, 3$). $\bar{p}$ is filtered pressure, ν and ρ stand for kinematic viscosity and water density, respectively. $\bar{S}_{ij}$ is the filtered fluid strain rate tensor and is denoted as:

$$\bar{S}_{ij} = \frac{1}{2}\left(\frac{\partial \bar{u}_i}{\partial x_j} + \frac{\partial \bar{u}_j}{\partial x_i}\right) \tag{3}$$

In Eq. (2), τ^s_{ij} represents the effects of the unresolved part as:

$$\tau^s_{ij} = \overline{u_i u_j} - \bar{u}_i \bar{u}_j \tag{4}$$

where τ^s_{ij} is obtained from the filtering process. Since the traceless form of τ^s_{ij} is preferred for the finite volume method, the deviatoric part of the SGS tensor is separated as:

$$\tau^s_{ij} = \tau^m_{ij} + \frac{1}{3}\tau^s_{kk}\delta_{ij} \tag{5}$$

where δ_{ij} is the Kronecker delta and τ^m_{ij} is traceless part of SGS tensor and modeled as $\tau^m_{ij} = 2\nu_{sgs}\bar{S}_{ij}$. The sub-grid scale eddy viscosity (ν_{sgs}) is defined as an artificial viscosity to consider the effects of the unresolved part. Finally, Eq. (2) is modified as follows:

$$\frac{\partial \bar{u}_i}{\partial t} + \frac{\partial \bar{u}_i \bar{u}_j}{\partial x_j} = -\frac{1}{\rho}\frac{\partial \tilde{p}}{\partial x_i} + g_i + 2\left(\nu + \nu_{sgs}\right)\frac{\partial \bar{S}_{ij}}{\partial x_j} \tag{6}$$

in which $\tilde{p}$ is produced by merging the difference part of Eq. (5) with the filtered pressure term as $\tilde{p} + \frac{1}{3}\tau^s_{kk}\delta_{ij}$.

2.2. Sub-grid scale models

The filtering procedure decomposes an arbitrary field $f(\mathbf{x})$ into two parts, including filtered $\bar{f}(\mathbf{x})$ and unresolved $f'(\mathbf{x})$. The resolved part is obtained numerically from the computational domain, while the unresolved part needs to be modelled by a closure model named Sub-Grid Scale (SGS) models. Accordingly, turbulent kinetic energy consists of resolved and sub-grid scale parts.

For the numerical filtering purpose, a characteristic length scale Δ is introduced, and the eddies with a larger length scale than Δ are taken into account by the grid size. Commonly, the characteristic length scale is determined by the cubic root of the cells' volume:

$$\Delta = \sqrt[3]{\Delta_x \Delta_y \Delta_z} \tag{7}$$

where Δ_x, Δ_y, and Δ_z are cell sizes in streamwise, spanwise, and azimuthal directions, respectively. Several SGS models have been developed to assess sub-grid scale kinetic energy. The following gives a description of two of these models:

2.2.1. Zero-equation SGS model

Smagorinsky [28] developed a primitive zero-equation SGS model, in which the Smagorinsky model, turbulent stress tensor τ^s_{ij} is related to the resolved strain rate tensor $\bar{S}_{ij}$ by an algebraic equation [28,29]. This model is based on the local equilibrium of TKE energy production and dissipation rate, where the SGS kinetic energy computed as:

$$ak_{\text{sgs}} + b\sqrt{k_{\text{sgs}}} + c = 0 \tag{8}$$

where for incompressible flow $a = C_{1\epsilon}/\Delta$, $b = 0$, and $c = 2C_k|\bar{S}|^2$. Additionally, C_k and $C_{1\epsilon}$ represent model coefficients which are obtained experimentally. This model has flaws due to the balance between SGS energy production and dissipation, being addressed in the next generation of SGS models.

2.2.2. One-equation SGS model

Yoshizawa and Hiriuti presented the primitive one-equation eddy viscosity model [30]. For considering the historical effects of k_{sgs} due to production, dissipation, and diffusion, a transport equation is adopted as:

$$\frac{\partial (k_{\text{sgs}})}{\partial t} + \frac{\partial (\bar{u}_j k_{\text{sgs}})}{\partial x_j} = \frac{\partial}{\partial x_j}\left[\left(\nu + \nu_{sgs}\right)\frac{\partial k_{\text{sgs}}}{\partial x_j}\right] + 2\nu_{sgs}\bar{S}_{ij}\bar{S}_{ij} - C_{2\epsilon}\frac{k^{3/2}_{\text{sgs}}}{\Delta} \tag{9}$$

where $C_{2\epsilon}$ is a model coefficient.

Both SGS models mentioned above use constant coefficients, thus known as static. Compared to dynamic SGS models, which adjust model coefficients dynamically, these models are more stable and require less computational effort. The effectiveness of the Smagorinsky (zero-equation) and k-equation (one-equation) models in addressing the problem of breaking solitary waves is evaluated in this paper.

Moreover, the sub-grid scale eddy viscosity is computed using $\nu_{sgs} = C_k \Delta \sqrt{k_{\text{sgs}}}$ in which C_k is a model coefficient. The coefficient values C_k and $C_{1\epsilon} = C_{2\epsilon}$ are taken as 0.094 and 1.048, respectively, which are common in different research areas [31].

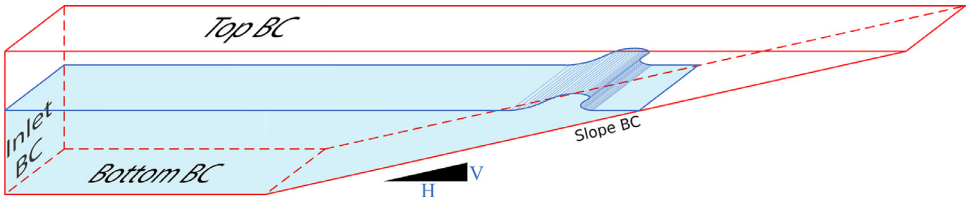

Fig. 1. Schematic wave domain with the name of boundaries, where Front and Back boundary conditions represent the vertical planes perpendicular to Inlet BC.

2.3. Volume of fluid method

The volume of fluid (VOF) technique is utilized to trackthe air-water interface in the discretized domain. Meanwhile, the fluid properties in each cell are identified by the occupied fraction of the cell. In this method, an advection equation is coupled with the governing Eqs. (1), (2) to evaluate the water surface evolution during the solution procedure:

$$\frac{\partial \alpha}{\partial t} + \frac{\partial \alpha u_j}{\partial x_j} = 0 \tag{10}$$

in which one indicator phase function (α) is defined as the portion of cells' volume occupied with the main phase fluid. Accordingly, a full cell, an empty cell, and an interface cell are indicated by $\alpha = 1$, $\alpha = 0$, and $0 < \alpha < 1$, respectively. Furthermore, fluid properties are characterized by the phase function in the Eulerian discretized domain. In general, the fluid density and viscosity of each cell are represented as follows:

$$\rho = \alpha \rho_w + (1 - \alpha)\rho_a \tag{11}$$

$$\mu = \alpha \mu_w + (1 - \alpha)\mu_a \tag{12}$$

where ρ_w, ρ_a, μ_w, and μ_a are the densities and viscosities of air and water, respectively.

2.4. Boundary and initial conditions

A domain is designed based on an experiment in which the solitary wave propagates. The system boundaries are depicted in the schematic specified domain 1. Slip conditions are considered as lateral boundaries to reduce the lateral effects (Back and Front BC). The atmospheric pressure and no-slip conditions, respectively, serve as the top and bottom boundaries. The wave generation is located at the Inlet boundary, as depicted in the Fig. 1, and the slope on the right side has the same conditions as the bottom boundary. Further details of the boundary conditions are presented in Tables 1, 2, 3. Moreover, a static state is postulated for the initial condition of the whole domain.

2.5. Numerical implementation

OpenFOAM is employed in this study to implement numerical computations. OpenFOAM is an open-source CFD toolbox that consists of a pack of C++ libraries to solve complex fluid flow problems. The readers are referred to Jasak [32] for more information on the finite volume approach used by OpenFOAM [32]. OpenFOAM contains a multiphase solver which solves the Navier-Stokes equation for two immiscible, incompressible phases, named interFoam. interFoam is extensively performed for modeling two-phase flows, including offshore and coastal problems, and its performance in LES was validated by Zhou et al. (2014) [26]. Also, Deshpande et al. (2012) evaluated the VOF method's performance in the solver used in this study [33].

The numerical domain is employed to resemble the propagation and breaking of a solitary wave with a height of $0.09m$ in a constant depth of $0.3m$ joining to a 1 : 15 (V: H) slope plane, Fig. 2. Due to the three-dimensional nature of eddies, a three-dimensional domain is adopted to simulate the eddies produced by the solitary wave breaking correctly [19,24–26,34,35]. However, due to computational cost limitations, the width of the domain adopts one-third of its experimental counterpart.

This domain consists of four longitudinal subdomains, tabulated in Table 4. These subdomains are chosen based on balancing the fine mesh required to observe the vortices in the breaking zone and computational cost. The numerical domain includes more than 9.5 million cells, which contain 99.9% polyhedra-type cells. However, the geometry of the problem dictates an unstructured mesh over the slope.

Table 1
Boundary conditions of velocity.

Boundary name	mathematical description
Inlet	velocities are prescribed as Dirichlet BCs based on related wave theory
Bottom	Dirichlet $u_i = 0$
Top	Flow out of the domain: $\partial u_i/\partial x_i = 0$ Flow into the domain: assigns a velocity based on the flux in the patch-normal direction [14]
Front/Back	$\partial u_i/\partial x_i = 0$ for streamwise and vertical directions $u_y = 0$ where y is spanwise direction

Table 2
Boundary conditions of pressure.

Boundary name	mathematical description
Inlet	sets the pressure gradient to the provided value such that the flux on the boundary is that specified by the velocity boundary condition. But, the BC overspecified if pressure formulation is presented in wave theory
Bottom	sets the pressure gradient to the provided value such that the flux on the boundary is that specified by the velocity boundary condition
Top	p_0 for outflow and $p_0 - 0.5\lvert u_i^2 \rvert$ for inflow
Front/Back	$\partial p/\partial x_i = 0$

Table 3
Boundary conditions of volume fraction (α).

Boundary name	mathematical description
Inlet	α is specified explicitly as a function of water surface based on related wave theory
Bottom	$\partial \alpha/\partial x_i = 0$
Top	$\partial \alpha/\partial x_i = 0$ for outflow and $\alpha = 0$ for inflow
Front/Back	$\partial \alpha/\partial x_i = 0$

Table 4
The subdomains range and minimum cells' size in each direction.

subdomain	zones	$\Delta x(m)$	$\Delta y(m)$	$\Delta z(m)$
1	$-14 < x < 0$	0.02	0.043	0.011
2	$0 < x < 1.5$	0.01	0.021	0.0055
3	$1.5 < x < 4.7$	0.005	0.011	0.0027
4	$4.7 < x < 7.5$	0.01	0.021	0.0055

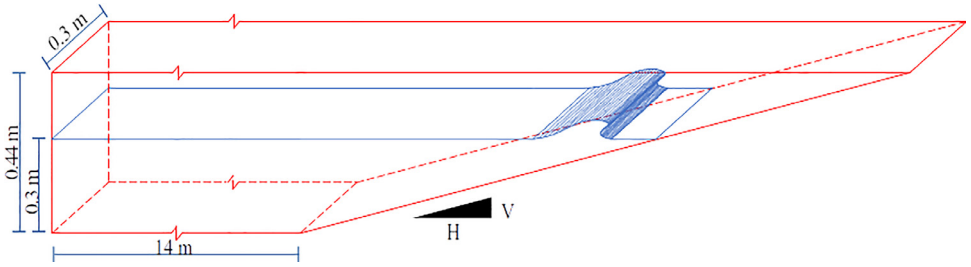

Fig. 2. Schematic numerical domain and its dimensions. The horizontal bottom joins 1:15 (V:H) slope at $x = 0$.

Table 5
Different spatial discretization with a fixed Courant value of 0.2.

test number	1	2	3	4	5	6
min $\Delta x(m)$	0.0043	0.005	0.0056	0.0063	0.0082	0.0131
min $\Delta y(m)$	0.0095	0.011	0.0123	0.0139	0.018	0.0289
min $\Delta z(m)$	0.0023	0.0027	0.0031	0.0034	0.0047	0.0071
Number of cells ($\times 10^6$)	≈ 11	≈ 9.5	≈ 8.6	≈ 7.7	≈ 5.8	≈ 3.7
NRMSE	finest	0.0024	0.0079	0.0198	0.0147	0.0333

3. Model assessment

This section assesses modeling validity in three stages: convergence, validation, and LES performance evaluation. All numerical model results are taken from a vertical longitudinal surface in the domain's middle to minimize the effects of lateral boundaries.

3.1. Convergence

The convergence tests consist of spatial and temporal parts. In the former, the results are investigated against different mesh sizes with a constant Courant number ($\mathrm{Co} = u\Delta t/\Delta x$), while in the latter, the Courant number changes with a fixed mesh size. Convergence was studied using the finest mesh size and the smallest Courant number as benchmarks. The Normalized Root Mean Square Error (NRMSE) criterion is used for this aim:

$$\mathrm{NRMSE} = \frac{\sqrt{\frac{\sum_{n=n_1}^{n_1+N}(\zeta_{\mathrm{finest,\ n}} - \zeta_n)^2}{N}}}{\zeta_{\mathrm{finest,\ max}} - \zeta_{\mathrm{finest,\ min}}} \tag{13}$$

where n is the counter of the peer value in the space domain, ζ is the studied property, and N is the total number of samples.

The numerical water surface results for different mesh sizes are compared to evaluate mesh adequacy. The convergence test is conducted for water surface changes within the whole simulated domain using the NRMSE criteria. The water surface (η) is adopted as ζ, in Eq. (13), which is determined as the locus of all points with $\alpha = 0.5$. The properties and NRMSE of different mesh sizes and Courant numbers are tabulated in Tables 5 and 6, respectively. In addition, the results are plotted in Figs. 3 and 4 in which h denotes the water depth.

As illustrated in Fig. 3, the results are approached the finest mesh size (Test 1), as long as mesh size decreases. Additionally, the dashed line and dotted line coincide, which means the results of Tests 1 and 2 are consistent. As shown in the subfigure, the NRMSE decreases in a roughly exponential relationship with the increasing number of cells. Hence the mesh size of Test 2 is adopted for the reference mesh size as it is close enough to the horizontal part of the computational cost graph.

The dependence of the numerical model on the Courant number is depicted in Fig. 4. A Courant of 0.2 is sufficiently close to the benchmark test (Test 1) to select its attributes for the ultimate model. Comparing Figs. 3 and 4 infers that Courant dependency in the high gradient water surface region is remarkable, whereas the mesh size affects the whole domain.

Table 6
Different temporal discretization tests, while in these bunch of tests, the mesh sizes are identical ($\Delta x = 0.005m$, $\Delta y = 0.011m$, $\Delta z = 0.0027m$).

test number	1	2	3	4
Courant number	0.15	0.2	0.5	0.8
NRMSE	finest	0.0028	0.0168	0.0332

3.2. Validation

In this section, the validation of numerical results is examined against theoretical values and experimental data. In the former, the water surface of the numerically propagated solitary wave is compared to its equivalent theoretical values using a constant water depth condition. Whereas, in the latter, the water surface of the numerical simulation is validated against laboratory results in the breaking zone [36].

3.2.1. Validation against theoretical values

In a numerical practice, the Boussinesq theory is used to generate a solitary wave using the BCs described in Section 2.4. The below function for adjusting the water surface at the inlet boundary is followed by the boundary condition for the phase function ($alpha$) [37,38]:

$$\eta = h + H\mathrm{sech}^2\left(\sqrt{\frac{3H}{4h^3}}(x - C_0 t)\right) \tag{14}$$

where H and C are wave height and celerity ($C_0 = \sqrt{g(h+H)}$). Besides, Boussinesq and Grimshaw's theories allow having a theoretical counterparts for propagating the wave, where the rst-order solitary wave theory of Grimshaw is defined as [39]:

$$\eta = h + h\left(\epsilon s^2 + \frac{3}{4}\epsilon^2 s^2\beta^2 + \epsilon^3\left(\frac{5}{8}s^2\beta^2 - \frac{101}{80}s^4\beta^2\right)\right) \tag{15}$$

where

$$\epsilon = \frac{H}{h}; s = \mathrm{sech}(\gamma(x - ct)); \beta = \tanh(\gamma(x - ct));$$
$$\gamma = \sqrt{\frac{3}{4}\epsilon}\left(1 - \frac{5}{8}\epsilon + \frac{71}{128}\epsilon^2\right) \tag{16}$$

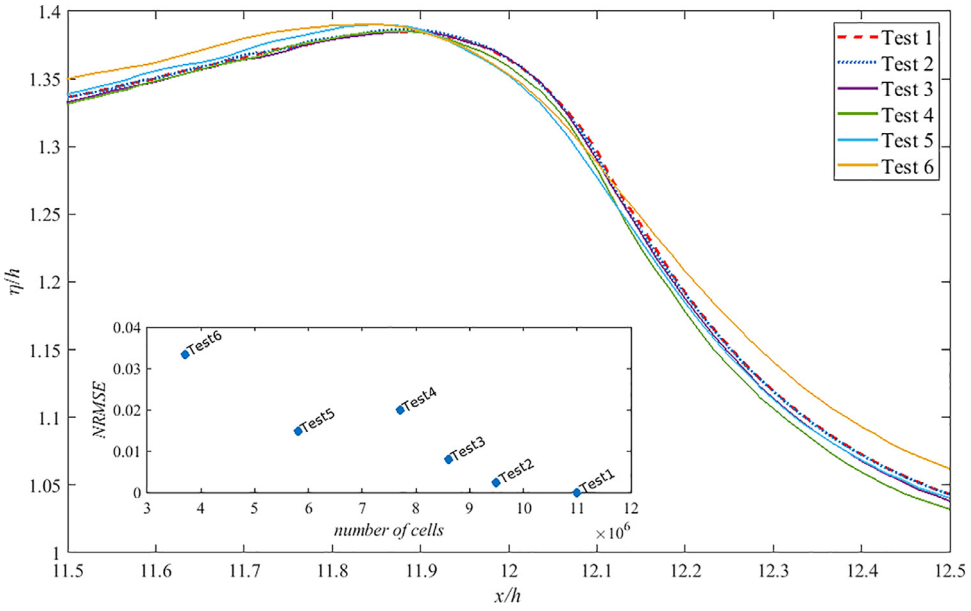

Fig. 3. Wavefront elevation of the stated tests is compared using the indicated space's horizontal axis at a certain moment.

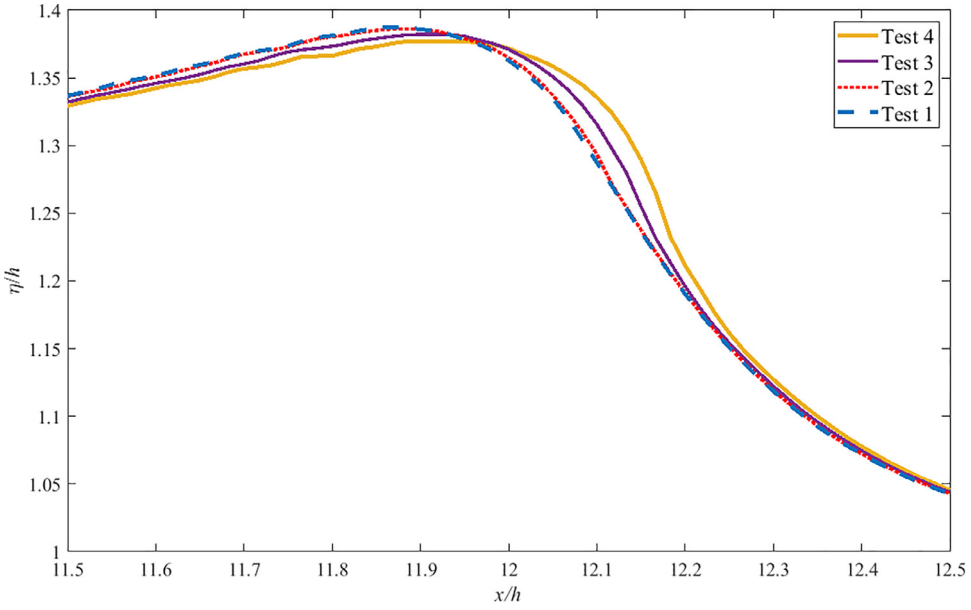

Fig. 4. The convergence dependency of the water surface to the Courant number; the wavefronts are compared in specified space and moment.

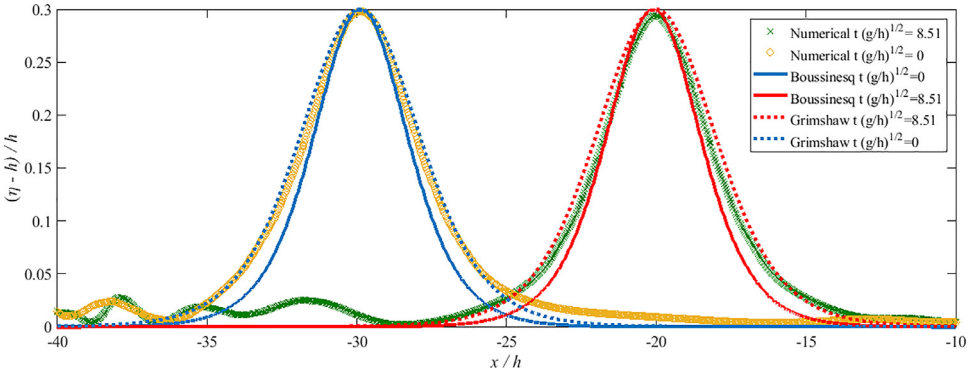

Fig. 5. The numerical model and theoretical solitary wave surface comparison. The dimensionless time variable is defined as $\sqrt{t(g/h)}$ when the wave crest is located in $x/h = -30$ at $\sqrt{t(g/h)} = 0$ [40]. The wave is generated at $x/h = -46.67$.

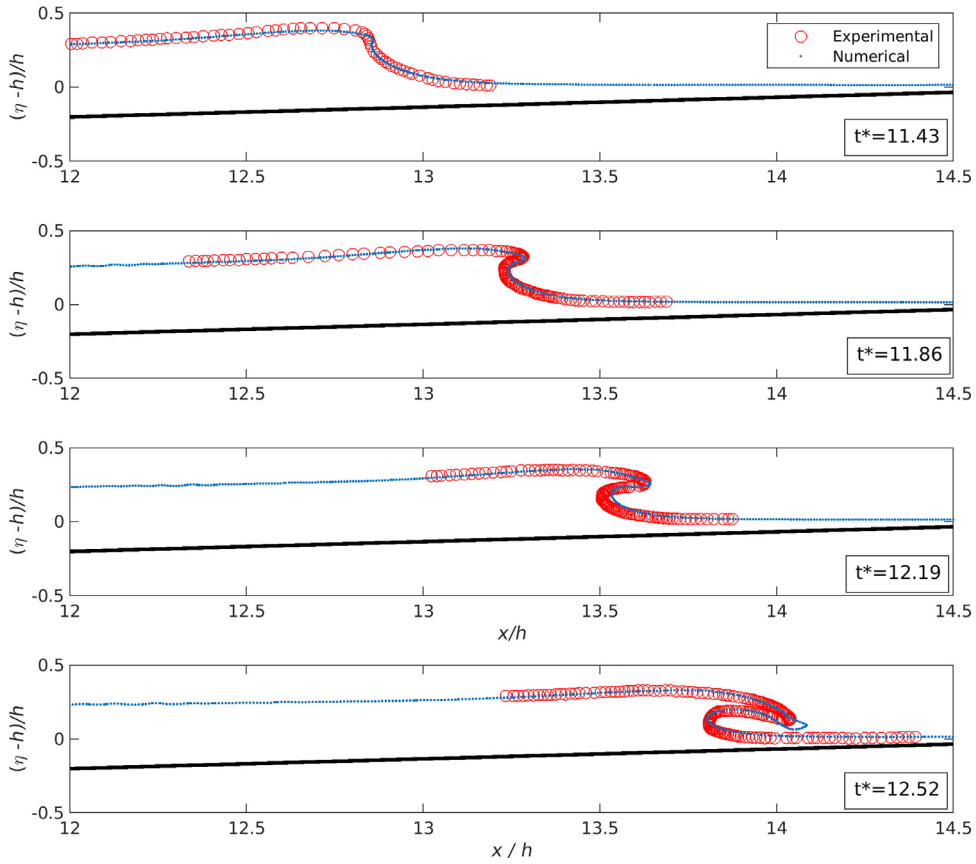

Fig. 6. The numerical results versus experimental data for water surface around breaking point. $t^* = 0$ is defined as when the crest of the wave across the join of slope and horizontal bottom ($x = 0$).

Fig. 5 illustrates the comparison of numerical simulation and theoretical values for two dimensionless times of $\sqrt{t(g/h)} = 0$and $\sqrt{t(g/h)} = 8.51$ when the wave crest is at $x/h = -30$ and $x/h = -20$, respectively. As is illustrated in Fig. 5, the numeric wave convects with the same celerity as the theory counterparts; meanwhile, less than a 1% change in the amplitude and the phase difference is observed between them.

3.2.2. Validation against experimental data

Li [36] provided water level images of four specific stages during a solitary wave breaking on a 1:15 slope. These results are widely used for numerical validation, as in this study. The numerical model results are compared with the experimental data and are illustrated in Fig. 6. The results show a good agreement between the experimental and numerical models in the breaking zone.

3.3. Performance assessment of LES

In the LES approach, the total turbulence consists of resolved and unresolved parts. The resolved part stems from a time-average velocity field and contains turbulence fluctuations due to large eddies. The instantaneous velocity is decomposed to the mean and fluctuations as:

$$\mathbf{u_i} = \langle \mathbf{u_i} \rangle + \mathbf{u_i'} \tag{17}$$

where '⟨⟩' represents time-average operator, $\langle \mathbf{u_i} \rangle$ is mean velocity, and $\mathbf{U}'$ is velocity fluctuation. The mean velocity and prime-squared mean Reynolds stresses ($\langle u_i' u_j' \rangle$) are directly obtain from a library of OpenFOAM and the resolved turbulent kinetic energy is calculated as follows:

$$k_{\text{res}} = \frac{1}{2}\left(\langle u_i' u_i' \rangle\right) \tag{18}$$

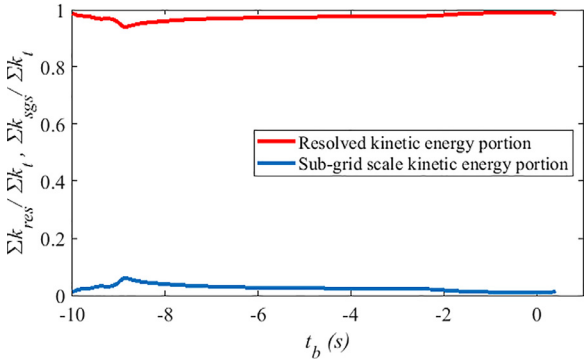

Fig. 7. Time series of k_{res} and k_{sgs} portion in the whole domain, while $t_b = 0$ is taken as the exact time of breaking (when the wavefront becomes vertical).

where u_i' is velocity fluctuation in different directions. As an estimation in LES, a good mesh empowers the numerical model to resolve most of the energy and a smaller part of TKE modelled by the SGS model. The total turbulence level is defined as summation of resolved kinetic energy (k_{res}) and the sub-grid scale turbulence (k_{sgs}), which are obtain from Eqs. (8), (9).

Fig. 7 illustrates the time series of $\Sigma k_{\text{res}}/\Sigma k_t$ and $\Sigma k_{\text{sgs}}/\Sigma k_t$ where Σk represents of instant summation of k in the whole domain. All in all, the results demonstrated that the mesh resolved more than 95% of turbulence levels.

4. Results and discussion

As mentioned in Section 1, breaking onset and wave collapsing have different physics. In the breaking process, which is the fo-

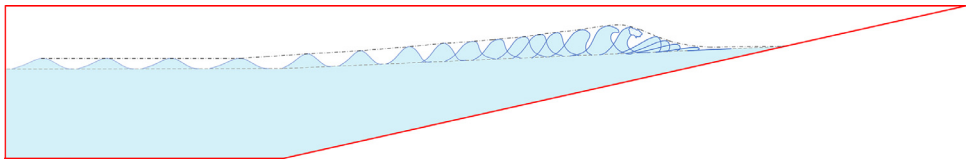

Fig. 8. The schematic figure for solitary wave evolution with time in a horizontal domain joining to a sloping plane. The dashed line shows the maximum solitary wave height envelope.

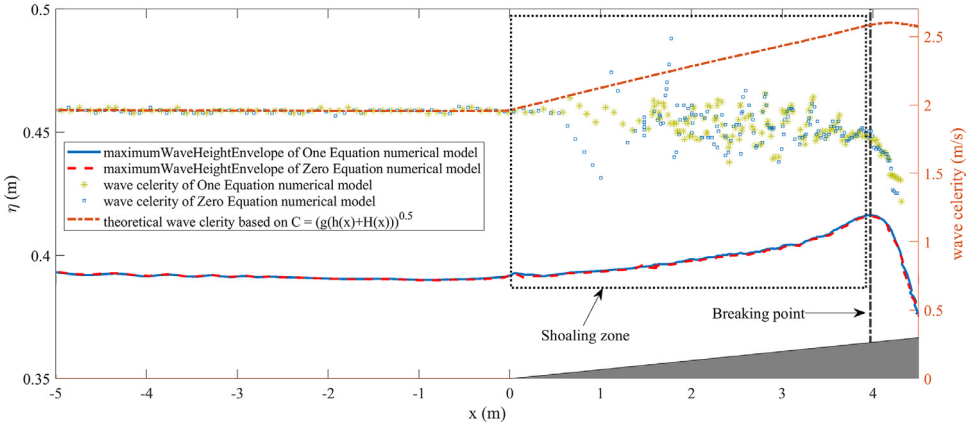

Fig. 9. Celebrities and maximum wave height envelope for both SGS models. The dashed line represents theoretical wave celerity $C_0 = \sqrt{g(H(x)+h(x))}$. The left vertical axis stands for the wave height, whereas the right one specifies the velocity scale. Noteworthy, the results of the theoretical wave celerity for both SGS models coincide (the red dash-dotted line). (For interpretation of the references to colour in this figure legend, the reader is referred to the web version of this article.)

cus of this study, the dynamics of wave motion lead to wave overturn at the breaking point. This study aims to evaluate the turbulent kinetic energy (TKE) and associated hydrodynamic events during breaking in the shoaling zone, which has both scientific significance and engineering value. As a solitary wave crosses the shoaling zone, the breaking process generates different sizes of vortices [24]. The large-scale turbulence is produced by the breakdown of these large vortices, leading to an increase in turbulence levels beneath the wave surface as the ratio of water depth to wave height decreases [41]. Furthermore, surface-generated turbulence occasionally dominates bed-generated turbulence, emphasizing the importance of evaluating the TKE in the breaking wave phenomenon [41,42].

Depending on breaking type, turbulence structures are convected and diffused by the wave by the breaking [9,11,12]. Farahani and Dalrymple [25] demonstrated that the turbulence structures move seaward under the spilling break, whereas they move in the other direction under the plunging break [25]. Moreover, the amount of energy dissipated by plunging breakers is considerable compared to spilling breakers. Therefore, this study conducts a numerical analysis to investigate the fate of TKE under a plunging solitary wave.

The model described in Section 2.1 was examined in Section 3 in light of both experimental data and the theoretical formulation. Section 3 provided a validation of the numerical model, and this section uses the validated model to elucidate plunging solitary waves in more detail.

A three-dimensional numerical simulation was used to investigate the turbulent flow structures under a laboratory-scale breaking solitary wave. The study begins by examining the celerity and maximum height envelope of the solitary wave in the shoaling zone. Two sub-grid scale (SGS) closure models, including zero- and one-equation models, were used to evaluate and compare the production and spread of TKE in the shoaling zone. The turbulence level and velocity fields were then assessed just before the wave collapsed. The last subsection examines the flow field characteristics before the wave collapses and parameterizes the breaking onset; two different kinetic criteria are examined: wave crest velocity and maximum surface particle horizontal velocity.

4.1. Solitary wave evolution on slope plane

Numerous studies have focused on the evolution of solitary waves moving along a flat or sloping plane [43–48]. One of the most well-known equations for describing wave height and wave velocity is the Boussinesq equation (Eq. (14)). However, these formulas were developed for a solitary wave propagating on a horizontal bottom. Some research focused on the evolution of solitary waves on a sloping beach where shoaling is the dominant phenomenon [46–49].

The simulation of the evolution of the solitary wave in the numerical flume is done in this study, which includes generation at the start of the 14-meter horizontal domain, crossing along the flume's section of constant water depth, shoaling on the 1:15 slope plane, and ultimately collapsing at the breaking point. Because of the direct relationship between the wave energy and wave height, comparing wave heights at various locations illustrates that the wave's energy remains conserved during propagation in the horizontal bottom section without any source or sink of energy, Section 3.2.1. The decrease in water depth within the shoaling zone affects wave height, and Fig. 8 schematically illustrates the shoaling process, wave breaking, and maximum wave height envelope. Since the comparison of both SGS closure models is the focus of this subsection, the results of wave celerity and maximum height envelope are examined (Fig. 9).

As is illustrated in Fig. 9, the wave celerity and height remains constant while propagating on the horizontal bottom. At the beginning of the shoaling zone, the envelope level fluctuates due to changes in the mesh size in transient between subdomains. The wave height increases continuously by crossing over the slope until it reaches the breaking point at the maximum envelope value. At the breaking point, the wavefront becomes vertical and overturns around $x = 4$. Beyond that point, the wave height reduces rapidly, which is not the concern of this study.

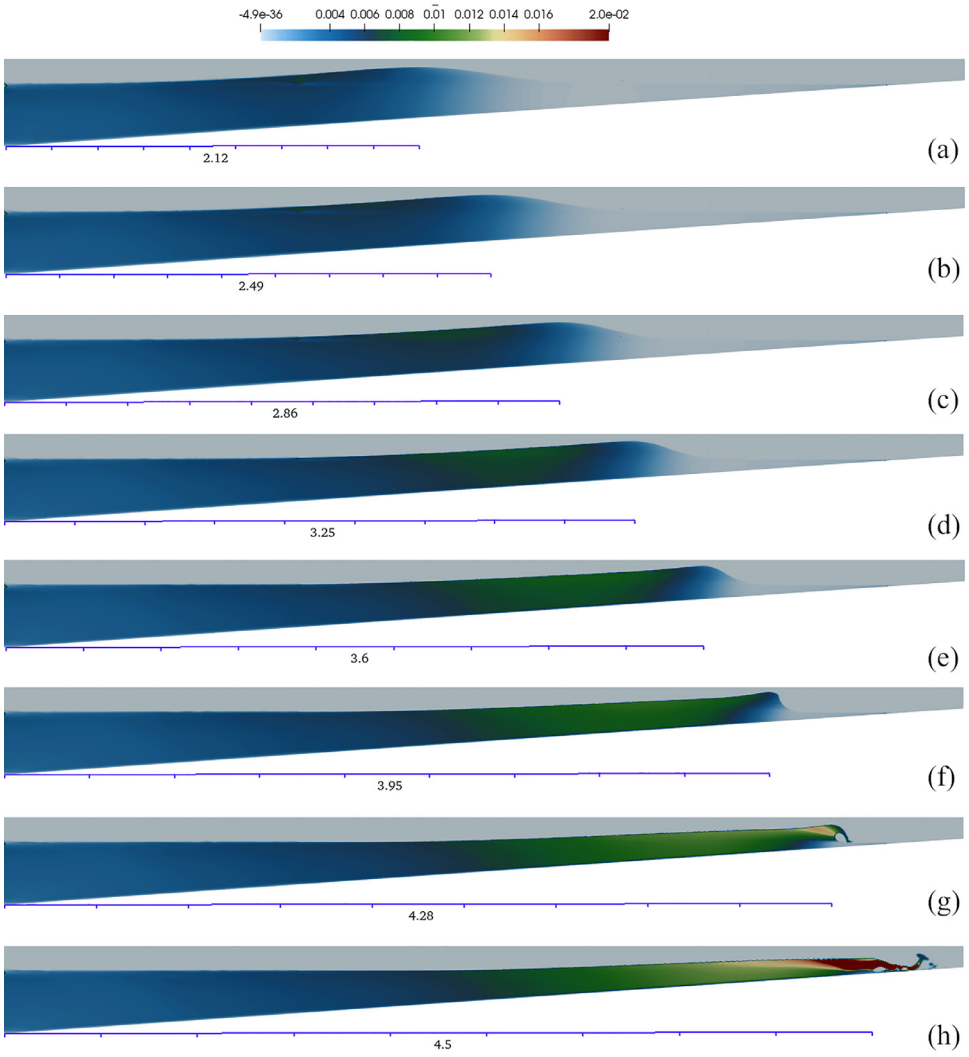

Fig. 10. Turbulent Kinetic Energy propagation in the domain obtained from the zero-equation SGS model for various time steps. Different parts are related to eight snapshots at (a) $t_b - 1$, (b) $t_b - 0.8$, (c) $t_b - 0.6$, (d) $t_b - 0.4$, (e) $t_b - 0.2$, (f) t_b, (g) $t_b + 0.2$, and (h) $t_b + 0.4$. Where t_b corresponds to when the front face of the wave crest becomes a vertical instance. The wave breaks at stage (f) when the front face of the wave crest becomes vertical, while (g) and (h) represent the collapsed wave.

The water surface profiles and wave velocity evolutions obtained from the two SGS models were compared, and the results indicate no significant discernible differences between the results of the two models. Furthermore, a comparison of the wave velocities resulting from simulation with their theoretical counterparts is depicted in Fig. 9. the theoretical and numerical celerity are shown in Fig. 9. In the former, the ratio of the wave crest displacement to the time step is adopted to calculate wave celerity. In the latter, the wave celerity is calculated theoretically using $C_0 = \sqrt{g(H(x) + h(x))}$, where $H(x)$ and $h(x)$ are the numerical model's wave height and water depth at a certain location, respectively.

The results depict that, within the shoaling zone, the numerically calculated wave celerity (C) is significantly less than its theoretical value (C_0). There are also some noticeable variations in the numerical findings' patterns; whilst the trend is downward at the beginning ($0 < x < 2$), it becomes inverse with a greater rate in the middle of the shoaling zone ($2 < x < 3$). This trend will eventually decline and eventually reach the breaking point. Grill et al. Grilli et al. [47] reached the same conclusions [47]. Similarly, Knowles and Yeh [49] compared the solitary wavelength and the slope length to identify their effects on wave height during shoaling [49]. All in all, the reasons for the difference between the theoretical and numerical results, as well as the numerical celerity variations, are summarized as follows:

- The non-dispersive assumption that underlies theoretical celerity (C_0) is untrue in the shoaling zone, while the solitary wave involves nonlinearity and frequency dispersion.
- The previously mentioned descending celerity approach is due to frequency dispersion.
- The dominance of wave nonlinearity on the dispersion effect justifies increasing wave velocity.

In addition, there is a tiny difference between the wave celerity calculated using the zero-equation and the one-equation models. This discrepancy causes a wave phase difference of about 0.02 s between the two SGS models.

4.2. Turbulent kinetic energy distribution through breaking proccess

As previously mentioned in the introduction, vortices are formed underneath the water's surface behind the crest of a breaking wave. These vortices break up and create turbulent structures that quickly spread throughout the water. The distribution of turbulent kinetic energy (TKE) varies depending on the type of wave breaking, with TKE either traveling landward or seaward. In this

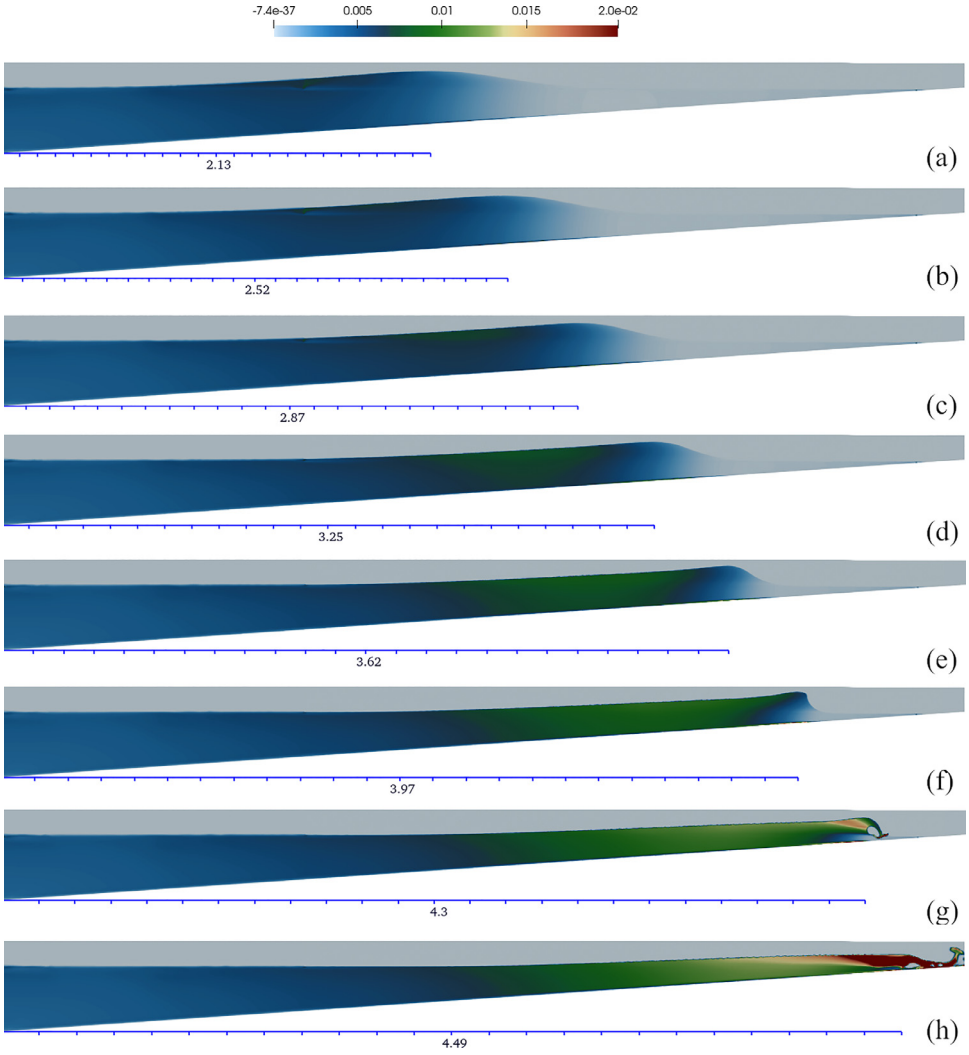

Fig. 11. Turbulent Kinetic Energy propagation in the domain obtained from the one-equation SGS model for various time sections.

subsection, the distribution of TKE under a plunging solitary wave will be compared using both the zero- and one-equation sub-grid scale (SGS) models.

Figs. 10 and 11 illustrate the qualitative spreading of the TKE under the solitary wave in the shoaling zone using the results of zero- and one-equation SGS models. The figures demonstrate the TKE intensity, wave crest position, and chronological order of the eight stages of the breaking process. At the initial breaking stage (stage a), the turbulence resulting from wave-bottom interaction is more intense than the TKE for the entire domain. As time passes, the surface-generated turbulence begins to penetrate the deeper layer of the water column and gradually dominates bottom-generated turbulence.

According to the qualitative results of the model, the region characterized by higher turbulence intensity (as represented by the color green in Figs. 10 and 11) expands downward and forward during the breaking process. This observation is consistent with the findings of Ting and Kirby in their 1995 study [11]. As a result, the higher-level turbulent structures dominate over the wave crest due to shoaling effects. Comparing the stage (h) of the two SGS models reveals that the one-equation model exhibits a higher rate of turbulence propagation than the zero-equation model.

For a more thorough analysis of the differences between the two SGS models, Fig. 12 quantitatively depicts dimensionless TKE profiles beneath the wave crest.

Since the TKE in the LES approach consists of resolved (k_{res}) and sub-grid scale kinetic energy (k_{sgs}), their profiles are contrasted in Fig. 12 in chronological order (subfigures (a) to (h)). To ensure a consistent vertical scale between 0 and 1, the dimensionless variable $(z - z_{\mathrm{bot}})/(\eta - z_{\mathrm{bot}})$ is chosen, where z_{bot} represents the bottom level beneath the wave crest. The wave celerity square ($C2$) also renders the TKE profiles dimensionless.

According to the models' outcomes, due to the absence of a boundary layer mesh for resolving smaller near-bed vortices, the portion of k_{sgs} is greater than that of k_{res}. Subsequently, the maximum values of k_{sgs} occur close to the bottom for both SGS models, whereas k_{res} decreases near the bottom.

Both simulations use an identical grid size, resulting in approximately similar k_{res} values during the primary stages (a) to (f). However, after the breaking process, $k_{\mathrm{res,One}}$ is found to be 6% greater than its zero-equation counterpart, indicating TKE convection (stage (h)).

The ratio of $k_{\mathrm{res}}/k_{\mathrm{sgs}}$ decreases over time, indicating that sub-grid scale models become increasingly important as the wave approaches the breaking point. Therefore, choosing an SGS model compatible with the characteristics of TKE transportation in the breaking phenomenon is crucial. However, for the collapsed stage (h), the resolved part of the TKE (k_{res}) grows in size until it overtakes the SGS part. It is deduced that in the surf zone, the k_{res} rises more rapidly than k_{sgs}.

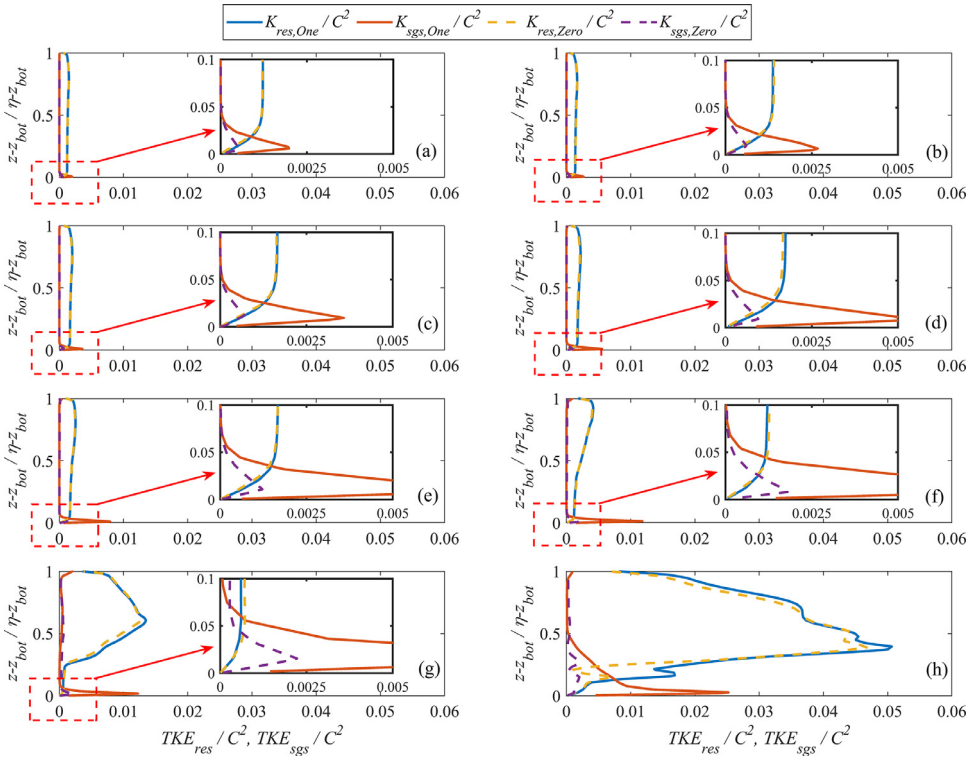

Fig. 12. Comparison of the TKE profiles under the wave crest between zero-equation and one-equation SGS models. Subscript Zero and One represent zero-equation and one-equation SGS models, respectively. (a) $t_b - 1$, (b) $t_b - 0.8$, (c) $t_b - 0.6$, (d) $t_b - 0.4$, (e) $t_b - 0.2$, (f) t_b, (g) $t_b + 0.2$, and (h) $t_b + 0.4$ where t_b is defined as the moment when front face of the wave crest becomes vertical.

Over time, $k_{sgs,One}$ increases beneath the wave crest, while $k_{sgs,Zero}$ remains roughly constant. The growing difference between $k_{sgs,One}$ and $k_{sgs,Zero}$ suggests that the SGS component of TKE is not adequately convected in the zero-equation model. In contrast, the upwind turbulence level (surface-generated turbulence) in the one-equation model characterizes the turbulent properties beneath the wave crest, which is consistent with experimental observations [11].

The maximum values of k_{res} and k_{sgs} for stages (a) and (h) are presented in Table 7 to assess the ordering of the TKE part before and after wave collapsing. The maximum values of TKE show that although the variation of k_{res} for both models is the same, the growth rate of k_{sgs} in the one-equation model is twice as fast as in the zero-equation model. Additionally, the $k_{sgs,One}$ is one order of magnitude larger than $k_{sgs,Zero}$.

The zero-equation model is based on the assumption of local equilibrium between turbulent production and energy dissipation rate, while the $k_{sgs,One}$ is calculated by a transport equation. As is demonstrated in reference [9], the nature of turbulent structures in the shoaling zone is inconsistent with local equilibrium assumption. Since most of TKE is resolved by the mesh and only a minor portion of TKE is modeled with the SGS models, both simulations imply the transportation of TKE. Nevertheless, a comparison of $k_{sgs,Zero}$ and $k_{sgs,One}$ indicates that the one-equation SGS model exhibits significantly superior performance in the transport of turbulence. Overall, the results of the one-equation SGS model show the advection and diffusion of TKE in the domain, which is consistent with the experimental findings [11].

Table 7
Maximum values of k_{sgs} and k_{res} for both SGS models.

stages	$k_{res,Zero}/C^2$	$k_{res,One}/C^2$	$k_{sgs,Zero}/C^2$	$k_{sgs,One}/C^2$
(a)	0.0015	0.0015	0.0005	0.002
(h)	0.0041	0.0042	0.0018	0.012

4.3. Flow field properties before wave collapsing

Following the breaking process, a new hydrodynamics field containing air entrainments is created by the wave overturns and events brought on by the collapse. On the other hand, the hydrodynamics before collapsing is related to the time history of the instabilities appearing beneath the surface. In the following, the results of the one-equation SGS model are used to analysis the flow field of four timesteps leading to the wave collapse ($t_b - 0.3$, $t_b - 0.2$, $t_b - 0.1$, and t_b).

Fig. 13 illustrates the details of the flow characteristics, including kinematic and turbulent properties, at three different levels (over the bottom, mid-depth, and beneath the water surface), as shown in subfigure (1). Additionally, two kinematic breaking criteria are employed, including the horizontal fluid velocity at the wave crest u_c and the maximum horizontal fluid velocity around the wavefront surface u_m. These criteria are depicted with vertical green dashed u_c and dotted u_m lines in Fig. 13.

4.3.1. Kinematic properties

The ratio of surface horizontal velocity to wave celerity, denoted as u/C, is employed to assess the kinematic properties. This reference is shown to compare the u_c and u_m criteria in Plot (2) of Fig. 13 [50]. Furthermore, the breaking moment (t_b) is identified as the point at which the wavefront becomes vertical. At this moment, a cusp is evident in the u/C graph at the breaking point, as depicted in subfigure (d).

Plots (5) and (6) show the horizontal and vertical velocities for each time step. Maximum values (u_m) occur ahead of the wave crest due to a phase difference between the horizontal velocity be-

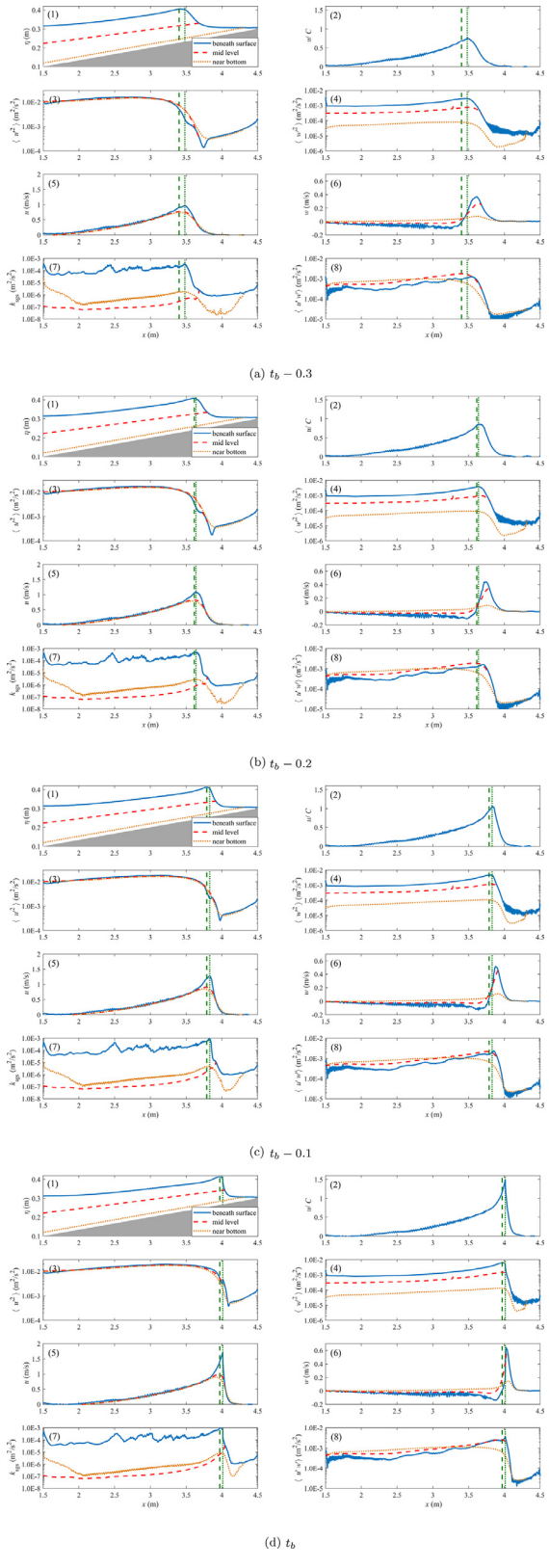

(a) $t_b - 0.3$

(b) $t_b - 0.2$

(c) $t_b - 0.1$

(d) t_b

Fig. 13. The flow field characteristics under breaking wave. The horizontal fluid velocity at the wave crest (u_c represented as green dashed line) and the maximum horizontal fluid velocity (u_m represented as green dotted line) around the wavefront surfaceare shown with the green vertical dashed and dotted lines, respectively. Different levels are depicted in subfigure (1) where the near bottom line is selected 2 *cm* upper than the bottom. (For interpretation of the references to colour in this figure legend, the reader is referred to the web version of this article.)

neath the water surface. The horizontal velocity, however, is synchronized with the water's surface at mid-level and close to the bottom. Notably, the horizontal velocity near the surface has higher values than at the mid-level and near the bottom, particularly at t_b.

In terms of vertical velocities, the slope of the w graph beneath the surface is greater than the slopes of the mid-level and over-bottom counterparts. Meanwhile, as it approaches t_b, the w graph becomes steeper. The azimuthal particle velocity graphs show that the inflection point of vertical velocities in each level occurs at the same location as u_m. Kinematic properties suggest that the maximum horizontal velocity criterion (u_m) is more appropriate for kinematic events in the shoaling zone than the horizontal fluid velocity at the wave crest (u_c). This finding is in agreement with the results of a previous study conducted by Varing et al. [50].

4.3.2. Turbulent properties

The streamwise axial Reynolds stress ($\langle u'^2 \rangle$) graphs (plots (3)) indicate a relatively uniform distribution in depth and have similar magnitudes within the breaking zone. In contrast, the vertical axial Reynolds stress ($\langle w'^2 \rangle$) graphs (plots (4)) show a two-fold decrease in magnitude with increasing depth. According to its definition (relation 18), the vertical distribution resolved kinetic energy (k_{res}) is mostly influenced by variations in $\langle w'^2 \rangle$.

Regarding the SGS component of TKE, plots (7) show that k_{sgs} has a significant value under the free surface. Since there is no boundary layer mesh, k_{sgs} is greater near the bottom than at the mid-level. Despite an increase in k_{sgs} near the breaking point, k_{res} is at least one order greater than k_{sgs}. Therefore, it is concluded that most TKE is carried by the resolved eddies. As a result, the numerical simulation is very close to DNS.

In terms of turbulent shear stresses (plots (8)), far from the breaking point, the near bottom shear stress $\langle u'w' \rangle$ is larger than the whole water column with the almost constant distribution, indicating the spreading of the surface-generated shear stresses to the deeper layers. Around the wave crest, the mid-level $\langle u'w' \rangle$ graphs increase slightly and dominate their near-bottom peer.

Notably, the turbulent properties' extremums occur at u_m, which indicates the superiority of u_m to u_c in evaluating the turbulent-related breaking phenomena.

5. Conclusion

This study employed a three-dimensional large eddy simulation to compare the performance of the zero- and one-equation subgrid scale models in simulating a plunging solitary wave. The accuracy of the numerical model in predicting wave celerity and free surface evolution was determined by validating it against analytical and laboratory results. The analysis suggests that both SGS models accurately predict the water surface and wave celerity during the wave propagation and shoaling processes, where no significant differences are observed between the models.

During the breaking process, the turbulence levels were studied using Turbulent Kinetic Energy (TKE), which includes resolved k_{res} and unresolved k_{sgs} components. The results demonstrated that both SGS models have maximum values of k_{sgs} near the bottom, while k_{res} decreases close to the bottom.

The resolved part of both models indicates similar values during breaking, while the growth rate of the unresolved part in the one-equation model is twice faster than in the zero-equation model. Furthermore, the maximum values of k_{sgs} in the one-equation model are at least an order of magnitude greater than its zero-equation model counterpart. As the wave approaches its collapsing point, the ratio $k_{\text{res}}/k_{\text{sgs}}$ decreases, indicating that,as the wave approaches the breaking point, the role of sub-grid scale models becomes increasingly important. Therefore, choosing an

SGS model compatible with the characteristics of TKE transportation in the breaking phenomena is crucial. The results of the one-equation SGS model, which agree with the experiment results, illustrate the advection and diffusion of the TKE in the domain. The fundamental assumption of the zero-equation model, on the other hand, is equivalent to turbulent kinetic energy production and dissipation, which restricts the accuracy of the transport of k_{sgs}. The comparisons indicate that the one-equation SGS model is more effective in capturing the small-scale turbulent motions during the breaking process.

Additionally, the results of the one-equation model were used to examine two kinematic breaking criteria: the horizontal fluid velocity at the wave crest u_c and the maximum horizontal fluid velocity around the wavefront surface u_m. Through the analysis of kinematic and turbulent characteristics, it was found that the u_m criterion is a better predictor of the onset of breaking waves compared to u_c.

Declaration of Competing Interest

The authors declare that they have no known competing financial interests or personal relationships that could have appeared to influence the work reported in this paper.

Acknowledgment

This paper acknowledges the funding support from the Research Institute for Sustainable Urban Development at the Hong Kong Polytechnic University (project numbers 1-BD86 and 1-BBWT).

References

[1] K.T. Kiger, J.H. Duncan, Annu. Rev. Fluid Mech. 44 (2012) 563–596.
[2] A. Triki, Ocean Eng. 133 (2017) 133–141.
[3] S. Mnassri, A. Triki, Ocean Eng. 236 (2021) 109368.
[4] A. Babanin, Breaking and Dissipation of Ocean Surface Waves, Cambridge University Press, 2011.
[5] F. Ardhuin, B. Chapron, F. Collard, Geophys. Res. Lett. 36 (6) (2009).
[6] K. Nadaoka, M. Hino, Y. Koyano, J. Fluid Mech. 204 (1989) 359–387.
[7] W.K. Melville, F. Veron, C.J. White, J. Fluid Mech. 454 (2002) 203–233.
[8] F.C. Ting, Coastal Eng. 53 (5–6) (2006) 441–462.
[9] F.C. Ting, J.T. Kirby, Coastal Eng. 24 (1–2) (1994) 51–80.
[10] F.C. Ting, Coastal Eng. 55 (6) (2008) 522–536.
[11] F.C. Ting, J.T. Kirby, Coastal Eng. 24 (3–4) (1995) 177–204.
[12] F.C. Ting, J.T. Kirby, Coastal Eng. 27 (3–4) (1996) 131–160.
[13] J.L. Lara, A. Ruju, I.J. Losada, Proc. R. Soc. A Math.Phys. Eng. Sci. 467 (2129) (2011) 1215–1242.
[14] P. Higuera, J.L. Lara, I.J. Losada, Coastal Eng. 71 (2013) 102–118.
[15] A. Rahmani, M. N. Moghim, M. R. Chamani, Inst. Civ. Eng. Proc. Marit. Eng. 176 (1) (2023) 14–30, doi:10.1680/jmaen.2021.013.
[16] B.E. Larsen, D.R. Fuhrman, J. Fluid Mech. 853 (2018) 419–460.
[17] B. Devolder, P. Troch, P. Rauwoens, Coastal Eng. 138 (2018) 49–65.
[18] B. Devolder, P. Rauwoens, P. Troch, Coastal Eng. 125 (2017) 81–94.
[19] E.D. Christensen, Coastal Eng. 53 (5–6) (2006) 463–485.
[20] R.A. Dalrymple, B. Rogers, Coastal Eng. 53 (2–3) (2006) 141–147.
[21] D. De Padova, R.A. Dalrymple, M. Mossa, J. Hydraul. Res. 52 (6) (2014) 836–848.
[22] D. De Padova, M. Mossa, S. Sibilla, J. Hydrodyn. 30 (1) (2018) 106–113.
[23] A. Mayrhofer, D. Laurence, B. Rogers, D. Violeau, Comput. Fluids 115 (2015) 86–97.
[24] E.D. Christensen, R. Deigaard, Coastal Eng. 42 (1) (2001) 53–86.
[25] R.J. Farahani, R.A. Dalrymple, Coastal Eng. 91 (2014) 261–279.
[26] Z. Zhou, J. Sangermano, T.-J. Hsu, F.C. Ting, J. Geophys. Res. Oceans 119 (10) (2014) 6952–6973.
[27] I. Kataoka, Int. J. Multiphase Flow 12 (5) (1986) 745–758.
[28] J. Smagorinsky, Mon. Weather Rev. 91 (3) (1963) 99–164.
[29] S. Huang, Q. Li, Int. J. Numer. Methods Eng. 81 (7) (2010) 835–865.
[30] A. Yoshizawa, K. Horiuti, J. Phys. Soc. Jpn. 54 (8) (1985) 2834–2839.
[31] A.K. Shukla, A. Dewan, Heat Mass Transf. 55 (3) (2019) 911–931.
[32] H. Jasak, Error analysis and estimation for the finite volume method with applications to fluid flows (1996).
[33] S.S. Deshpande, L. Anumolu, M.F. Trujillo, Comput. Sci. Discovery 5 (1) (2012) 014016.
[34] P. Lubin, S. Glockner, J. Fluid Mech. 767 (2015) 364–393.
[35] P. Lubin, O. Kimmoun, F. Véron, S. Glockner, Eur. J. Mech.-B/Fluids 73 (2019) 144–156.
[36] Y. Li, Tsunamis: Non-Breaking and Breaking Solitary Wave Run-Up, California Institute of Technology, 2000.
[37] R.G. Dean, R.A. Dalrymple, Water Wave Mechanics for Engineers and Scientists, Vol. 2, World Scientific Publishing Company, 1991.
[38] D.G. Goring, Tsunamis–the propagation of long waves onto a shelf(1978).
[39] R. Grimshaw, J. Fluid Mech. 42 (3) (1970) 639–656.
[40] C.E. Synolakis, The runup of long waves (2007).
[41] B. Ruessink, J. Phys. Oceanogr. 40 (12) (2010) 2696–2712.
[42] G. Voulgaris, M. Collins, Mar. Geol. 167 (1–2) (2000) 167–187.
[43] J. McCowan, London Edinb. Dublin Philos.Mag. J. Sci. 32 (194) (1891) 45–58.
[44] W.H. Munk, Ann. N. Y. Acad. Sci. 51 (3) (1949) 376–424.
[45] J.W. Daily, S.C. Stephan Jr., Coastal Engineering Proceedings (3) (1952). 2–2
[46] C.E. Synolakis, J.E. Skjelbreia, J. Waterway Port Coastal Ocean Eng. 119 (3) (1993) 323–342.
[47] S. Grilli, R. Subramanya, I. Svendsen, J. Veeramony, J. Waterway Port Coastal Ocean Eng. 120 (6) (1994) 609–628.
[48] S.T. Grilli, I.A. Svendsen, R. Subramanya, J. Waterway Port Coastal Ocean Eng. 123 (3) (1997) 102–112.
[49] J. Knowles, H. Yeh, J. Fluid Mech. 848 (2018) 1073–1097.
[50] A. Varing, J.-F. Filipot, S. Grilli, R. Duarte, V. Roeber, M. Yates, Coastal Eng. 164 (2021) 103755.